Contrib Mineral Petrol (2007) 153:743–760
DOI 10.1007/s00410-006-0175-3

ORIGINAL PAPER

Patterns of fluid flow in the contact aureole of the Late Miocene Monte Capanne pluton (Elba Island, Italy): the role of structures and rheology

Federico Rossetti · Francesca Tecce · Andrea Billi · Mauro Brilli

Received: 5 June 2006 / Accepted: 11 December 2006 / Published online: 9 January 2007
© Springer-Verlag 2007

Abstract Fluid–rock interaction was investigated in the inner aureole of the Late Miocene Monte Capanne pluton on Elba Island (Tuscany, central Italy) by integrating structural, petrological, fluid inclusion, and stable isotope analyses. In the north-western sector of the aureole (Procchio–Spartaia area), calc–silicates alternate with nearly pure carbonate layers at the metre scale. Close to the pluton, the prograde metamorphic sequence includes calc–silicates that transition within a few metres to overlying nearly pure calcite marbles. The calc–silicates are extensively metasomatised to form massive wollastonite-grossular-bearing exoskarn. The mineralogical assemblage found in the marbles and the unshifted carbon and oxygen isotopic ratios in calcite attest that the fluid phase was internally buffered. On the other hand, the calc–silicates constituted channels for infiltration of disequilibrium fluids of magmatic origin. Fluid infiltration was enhanced by hydrofracturing and structurally-controlled by existing planar anisotropies in calc–silicates (layering and lithological boundaries). At the metamorphic peak (~600°C and 1.5–2 kbar), the marble–calc–silicate interface acted as a barrier to fluids exsolved from the crystallising intrusions, separating two different flow patterns in the inner aureole: a high fluid–flux region on its higher grade side (Wol-zone) and a low fluid–flux region on the lower-grade side (Cpx zone). Results of this study: (1) documented that fluid pathways in the aureole rocks at the top of the pluton were largely horizontal, controlled by the lithological layering and the pluton–host rock contact; and (2) elucidated the primary control exerted by the structural and rheological properties of the host rocks on the geometry of fluid flow during pluton emplacement.

Communicated by J. Hoefs.

F. Rossetti (✉) · A. Billi
Dipartimento di Scienze Geologiche, Università Roma Tre, Largo S. Leonardo Murialdo, 1, 00146 Rome, Italy
e-mail: rossetti@uniroma3.it

F. Tecce · M. Brilli
Istituto di Geologia Ambientale e Geoingegneria, CNR, 00185 Rome, Italy

Introduction

Emplacement and cooling of magmas at shallow crustal levels are usually associated with the release of a great amount of fluids into the surrounding host rocks (e.g. Norton and Knight 1977; Hanson 1995; Oliver 1996). In such a context, fluids constitute an important medium for mass and heat exchange between the intruding magma and the country rocks, thus influencing both the regimes of contact metamorphism and the extent of metasomatic alteration (e.g. Nabeleck et al. 1984; Ferry and Dipple 1992; Jamtveit et al. 1993; Cartwright and Buick 1996; Buick and Cartwright 2002). Fluid flow patterns in contact aureoles also control the formation of ore deposits (e.g. Velsker 2004) and drive shallow geothermal systems (e.g. Dickson and Fanelli 2004).

Fluid–rock interactions in contact with aureoles mostly depend upon the balance between fluid production, thermal regime, composition and permeability of the host rocks (e.g. Hanson 1995; Dipple and Ferry 1996; Baumgartner et al. 1997; Connolly 1997; Cartwright 1998; Cui et al. 2001). Alteration of stable

isotope ratios and progress of mineral reactions are commonly used to infer the large-scale predominant direction of fluid flow and the extent of mass transport in contact aureoles (e.g. Nabelek et al. 1984; Baumgartner and Ferry 1991; Ferry and Dipple 1992; Cartwright and Buick 1996; Cook and Bowman 2000; Ferry et al. 2002). Therefore, knowledge of the permeability structure of the country rocks is an essential prerequisite for reconstructing hydrologic factors controlling the advective fluid flow during contact metamorphism. This is because geological fluid flow systems typically occur through heterogeneous and anisotropic media and are usually structurally controlled (e.g. Oliver 1996). The structural control of fluid flow is dependent upon the interplay between intrinsic parameters such as lithological boundaries and imposed processes such as deformation (fracturing and/or shear zones), both of which favour fluid channelisation (e.g. Dutrow and Norton 1995; Oliver 1996; 2001; Cartwright 1998). The structural setting and the deformation history of the pluton–host rock contact regions are thus expected to exert a pivotal role in controlling the hydrodynamics of contact metamorphism during active magma intrusion (e.g. Hanson 1995).

The purpose of this paper was to assess the permeability structure and hydrological history of the inner aureole of the Late Miocene Monte Capanne pluton on Elba Island (Tuscany, Central Italy) (Figs. 1, 2). Structural, petrological, fluid inclusion and stable isotope analyses were integrated to identify the composition, source and infiltration mechanism of the fluids promoting skarn mineralization at the intrusion–host rock contact. By focusing on distinct generations of veins that record the fluid–rock interaction history of the metamorphic host rocks during pluton emplacement, we identified two distinct generations of fluids of different composition, age, and origin: an early generation derived from the crystallising intrusive body and a late one derived from an external (meteoric) fluid source. The implications of these data in the framework of the active geothermal systems of southern Tuscany are also discussed.

Geological background and the local geology

The Monte Capanne pluton is part of the intrusive complex of western Elba Island (Dini et al. 2002; Rocchi et al. 2002 and references therein), belonging to the Neogene-Quaternary Tuscan Magmatic Province of Central Italy (Marinelli 1967; Innocenti et al. 1992) (Fig. 1). This magmatic suite is composed of dominantly acidic intrusives and cogenetic volcanic products, spanning from Middle Miocene in Corsica to Late

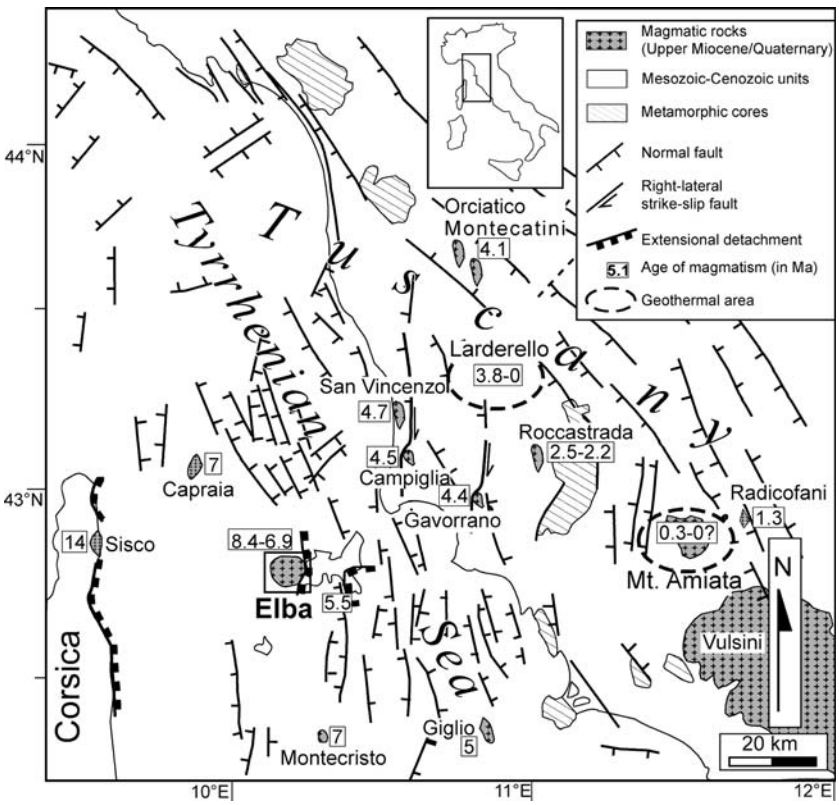

Fig. 1 Synthetic tectonic map of the inner sector of the Northern Apennine chain (modified and re-adapted after Jolivet et al. 1998) with location of the study area. The main products of the Tuscan Magmatic Province are also indicated (after Dini et al. 2002 and references therein)

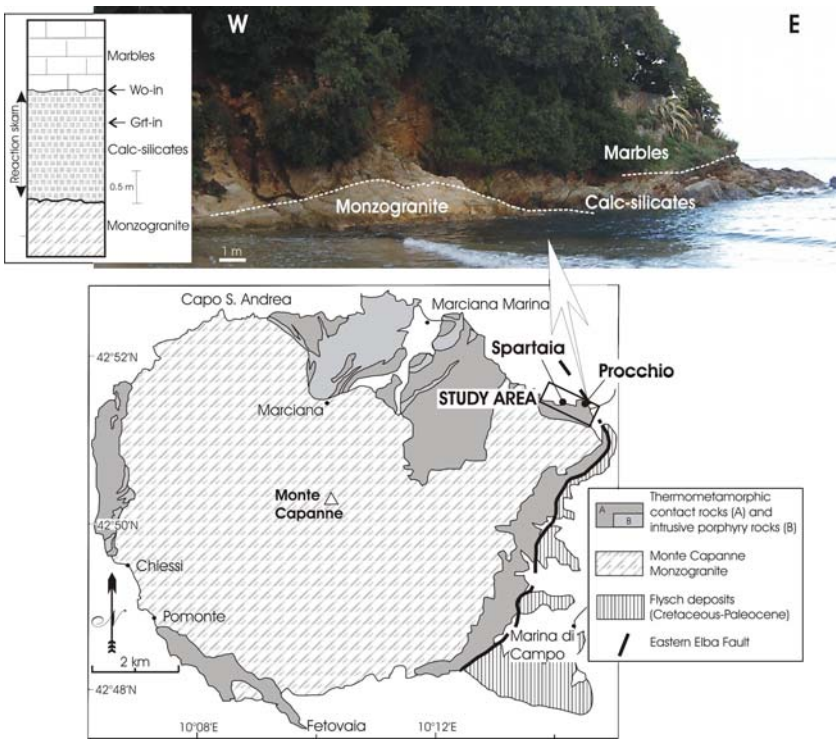

Fig. 2 *Bottom* Geological sketch map of western Elba Island (modified and re-adapted after Rocchi et al. 2002 and references therein) where locations of the studied exposures are indicated. *Top* The pluton–host rock contact exposed at Procchio. The *column to the left* shows the litho-stratigraphic section and the metamorphic mineral zonation as defined along a traverse perpendicular to the metamorphic layering close to the pluton–host rock contact

Pleistocene in the Tuscan region (e.g. Serri et al. 1993; Peccerillo 1999; Dini et al. 2005), that accompanied the eastward-migrating extensional collapse of the Apennine chain (e.g. Carmignani et al. 1994; Jolivet et al. 1998) (Fig. 1). Astenosphere upwelling and extensive crustal underplating of mantle-derived magmas is commonly thought to be the main heat source for the Tuscan magmatism. This has been interpreted as having derived from mixing between crustal and mantle sources with different degrees of hybridisation (Serri et al. 1993; Dini et al. 2002 and references therein). In southern Tuscany, a large-scale positive thermal anomaly occurs in the active geothermal areas of Larderello and Mount Amiata, where emplacement of Pliocene–Pleistocene intrusives (Dini et al. 2005) is responsible for extensive mesothermal fluid circulation and mineralization (e.g. Gianelli et al. 1997; Batini et al. 2003) (Fig. 1).

Elba Island is made of a complex stack of units, emplaced during the Apennine orogenic phase and consisting of both continental and oceanic-derived units (Trevisan 1950; Barberi et al. 1967; Bortolotti et al. 2001). Emplacement of numerous hybrid-anatectic intrusives accompanied the collapse of the orogenic nappe pile during multiple magma inputs spanning from about 8 to 5 Ma (Dini et al. 2002 and references therein). The composite Monte Capanne monzogranite pluton is the most important of these intrusive bodies that discordantly intruded the tectonic nappe stack of western Elba (Barberi et al. 1967; Dini et al. 2002) (Fig. 2). Pluton–host rock contacts define a general asymmetric structure. Steep magmatic and solid state foliation attitudes occur in the western and southern sectors of the pluton, whereas shallow-dipping foliations occur along the northern and eastern sectors (Boccaletti and Papini 1989; Boullin et al. 1993). The host rocks consist of a metamorphic aureole developed at the expense of an ophiolite-bearing tectonic sequence (complex IV and V in Trevisan 1950). This consists of mafic and ultramafic rocks alternating with shales, marls and limestones, from the Jurassic to Paleogene (Bortolotti et al. 2001 and references therein). Presently, no precise quantitative constraint exists on the *P*–*T* conditions associated with thermal metamorphism during emplacement of the Monte Capanne intrusion. However, peak temperatures of 600–700°C at $P < 2$ kbar have been proposed in the literature (e.g. Barberi and Innocenti 1965; Dini et al. 2002).

Outcrop characteristics: structures, mineralogy and textures

This paper focuses on the fluid evolution in the thermal aureole cropping out along the north-eastern margin of the Monte Capanne intrusive body. Observations and data are from a transect running from the Procchio to the Spartaia localities (Fig. 2). The general geology of

the study area was described in detail by Barberi and Innocenti (1965) and will be summarised here, also taking into account the new field data collected in this study. The pluton–host rock contact is almost flat-lying. Subvertical dykes cutting across the overlying metamorphic host rocks (Spartaia area) suggest that these exposures are likely located near the intrusion roof. In the Procchio area, the contact-metamorphosed host rocks consist of overlying, thinly-bedded, nearly pure marbles passing to underlying calc–silicate layers and metapelites hosting a discontinuous (up to 2 m thick) wollastonite-bearing exoskarn at the intrusion–wall rock contact (Fig. 2). The metamorphic parageneses and the mineral zonation are typified by the occurrence of Ca-clinopyroxene in marbles and by the appearance of the wollastonite isograd as the pluton–host rock contact is approached. In the innermost part of the aureole, the appearance of the grossular isograd is also observed (Fig. 2).

Structures in the host rocks consist of a transpositive, bedding-parallel, planar fabric developed during a nearly coaxial, vertical shortening. This foliation (S_p) is axial planar to nearly isoclinal folds, with average strike N170° and dip 10–15° to the west. Folding of late-segregated leucocratic dykes is also observed (Fig. 3a). The overlying marbles show a well-defined planar foliation, which transposes an original layering. The occurrence of centimetre-thick calcite boudins is frequent in the marble matrix (Fig. 3b). In thin sections, the marbles show an overall isotropic and well annealed granoblastic texture, defined by modally abundant calcite in association with minor Ca-clinopyroxene and K-feldspar (Fig. 3c).

The underlying calc–silicate rocks consist of banded granofelses layered to on a millimeter–centimetre scale, including boudins of biotite-bearing metapelites (Fig. 3d). Biotite mostly forms selvages around plagioclase, seldom associated with cordierite, andalusite and K-feldspar xenoblasts (Barberi and Innocenti 1965). The calc–silicates contain a wide variety of Ca-rich silicates (wollastonite, plagioclase, Ca-clinopyroxene, grossular, vesuvianite and scapolite), sometimes associated with K-feldspar. When present, carbonate minerals consist of calcite. Traces of graphite were also found in thin sections, but most of the calc–silicates are devoid of graphite. Three main calc–silicate types were identified in the Procchio area: (1) garnet free, Ca-clinopyroxene-bearing, green calc–silicates; (2) grossular-rich, pink calc–silicates, and (3) wollastonite-bearing, pale calc–silicates (Fig. 3d). The primary (peak metamorphic) assemblage consists of grossular (Grs_1) + Ca-clinopyroxene + anorthitic plagioclase + wollastonite. In the examined thin sections, the calc–silicate mineral assemblages are systematically devoid of quartz (see also Barberi and Innocenti 1965). Garnet typically forms poikiloblasts up to 3 cm in diameter, typically hosting Ca-clinopyroxene as the main mineral inclusion. Textures of the high-grade minerals in the calc–silicate samples systematically show straight grain boundaries and elongated polygonal grains (Fig. 3e).

The vein systems and the fracture systematics

Both foliation-parallel and foliation-perpendicular vein systems cross-cut the calc–silicate rocks exposed in the Procchio area. Foliation-parallel veins are the more prominent and their vein-filling minerals consist of grossular-wollastonite intergrowths in a matrix of coarse-grained vesuvianite crystals (Fig. 4a, b). These veins generally have planar margins and are continuous for distances up to 1 m, commonly associated with wollastonite-bearing alteration halos. A notable increase in the garnet grain size occurs in the calc–silicate beds, where radiating wollastonite blades coexist with poikiloblastic vesuvianite (Fig. 4b). These portions of the calc–silicate beds form typical bands at the layer interfaces, where poikiloblastic vesuvianite crystals dominate. In contrast, the wollastonite crystals typically occur at the vein-host rock interface (Fig. 4c). Small (up to 2 cm in width), foliation-perpendicular veins are usually observed to depart from the main subhorizontal (i.e. foliation-parallel) vein array (Fig. 4a, d). These veins are commonly filled with mineral associations similar to those filling the foliation-parallel veins (vesuvianite + garnet (Grs_2) ± wollastonite). These vein sets generally have mutual overprinting relationships with the foliation-parallel veins (Fig. 4d, e); even if some later foliation-perpendicular garnet- and epidote-bearing vein arrays also occur. Most of the vein arrays occurring in the calc–silicate rocks do not propagate through the overlying marbles, abutting against the marble–calc–silicate interface, where they form subhorizontal vein systems. Bedding-perpendicular veins tend to flatten when approaching the marble–calc–silicate contact, attesting that the marble–calc–silicate interface constituted a main rheological boundary, which separated the ductile-deformed marbles from the underlying heavily fractured calc–silicates (Fig. 4f). Texturally late, subvertical quartz-bearing veins were also found both in marbles and calc–silicates. Two main generations were observed: (1) an early, hydrothermal generation consisting of massive grey quartz (hereafter referred to as Qtz_1 veins; Fig. 5a), and (2) a later generation made of clean quartz dominantly found in the marbles (hereafter referred to as Qtz_2; Fig. 5b).

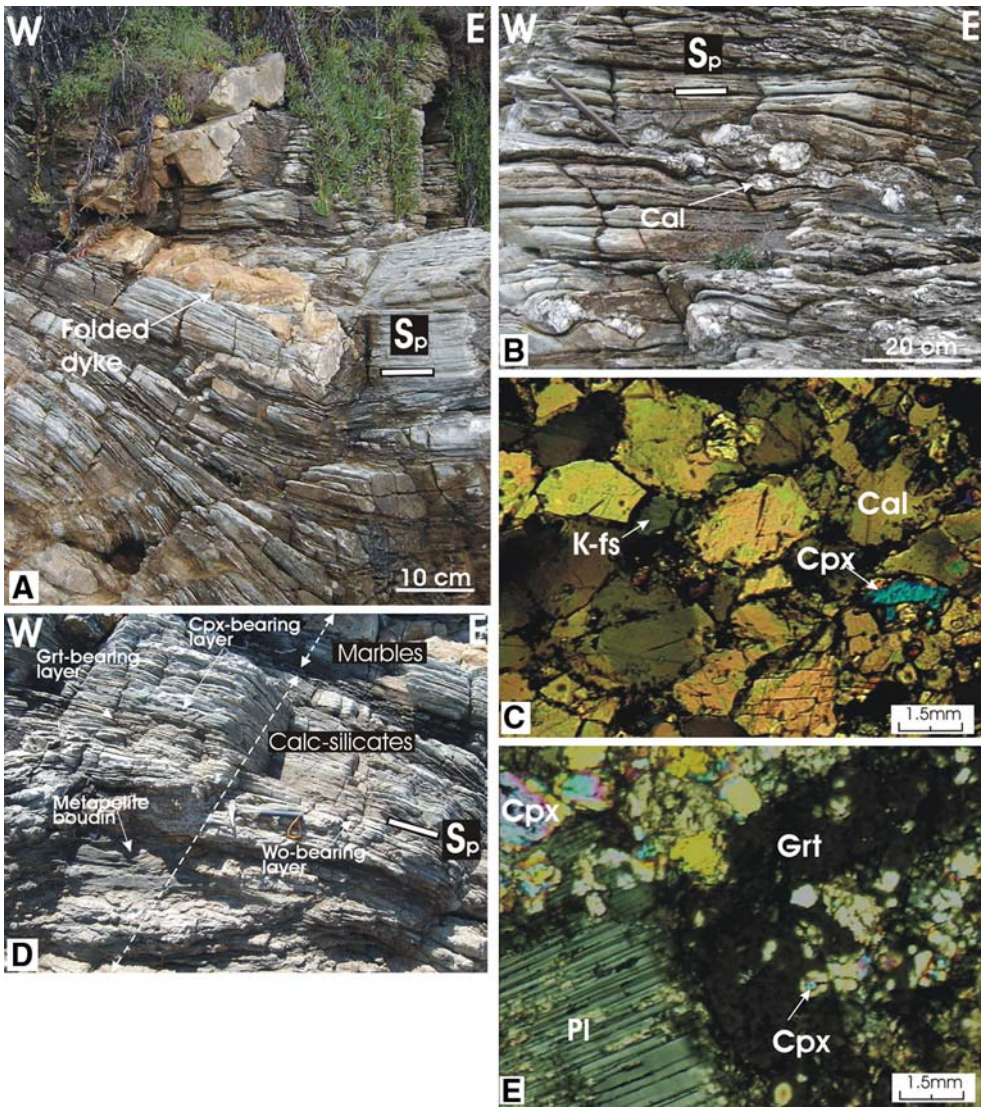

Fig. 3 Characters and textures of the marble–calc–silicate exposure at Procchio. **a** Overlying thinly foliated Cpx-bearing marbles. The foliation (S_p) is axial planar to nearly isoclinal folds refolding late-segregated dykes. **b** Marble exposures showing internal layering with intrafoliar calcite boudins. **c** Photomicrograph showing peak mineralogical assemblages in the overlying marbles, typified by coexisting calcite (*Cal*)-Ca-clinopyroxene (*Cpx*)-K-feldspar (*K-fs*) associations (*crossed polars*). **d** The marble–calc–silicate transition. The underlying calc–silicate rocks consists of dominant grossular-wollastonite-bearing granofelses. Minor metapelite layers are also found. **e** Photomicrograph showing peak mineralogical assemblages in the underlying calc–silicates. Coexisting garnet (*Grt*)-plagioclase (*Pl*)-Ca-clinopyroxene (*Cpx*) associations mark the metamorphic foliation in calc–silicates. Primary garnets (peak metamorphic) typically consist of coarse-grained poikiloblasts, with Cpx grains hosted as main inclusions (*crossed polars*)

The fracture pattern occurring in calc–silicates is poorly systematic with major sets striking ~N60°, ~N100°, and ~N170° (Fig. 5c). Fractures are dominantly steeply dipping (dip > 70°); however, low-angle fractures also occur. The fracture crosscutting relationships (i.e. as observed in plane view) mostly consist of X-type, +-type, and Y-type intersections (e.g. Pollard and Aydin 1988). X-type and +-type intersections are characterized by either continuous (i.e. non-abutted) or discontinuous (i.e. abutted) fractures. In the case of discontinuous fractures, we observed no preferential patterns for the abutting relationships, i.e. differently oriented fractures mutually abut (Fig. 5d). In marbles, fractures are nearly vertical and poorly systematic with major sets averagely striking N10°, N60°, and N100° (Fig. 5e). Fractures are rarely mineralised. The fracture crosscutting relationships consist of X-type, +-type, and Y-type intersections similar to those observed in the underlying calc–silicate rocks (Fig. 5f).

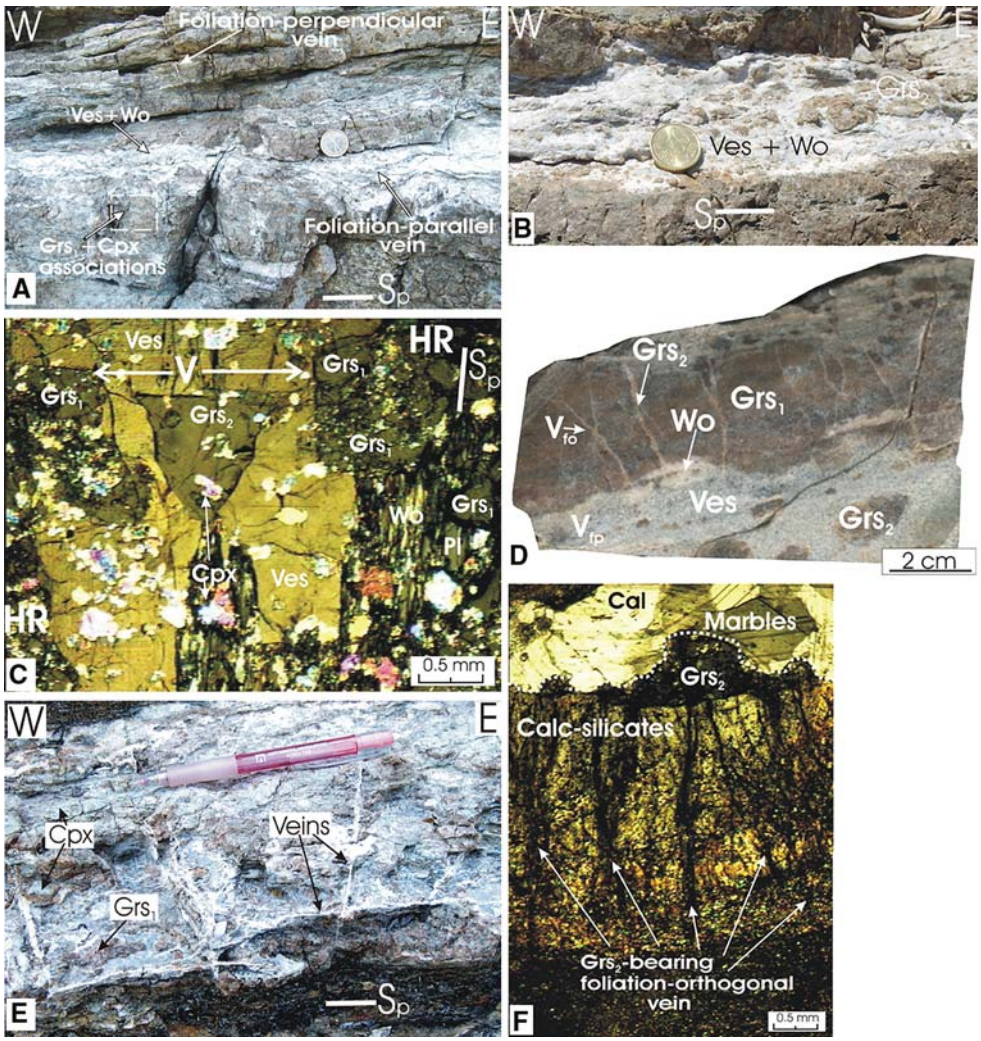

Fig. 4 Vein textures at the metamorphic peak in the calc–silicates at Procchio. **a** Centimetre-scale foliation-parallel, vesuvianite-wollastonite(*Ves-Wo*)-bearing veins associated with subordinate foliation-perpendicular ones. These veins cut through the earlier Grs_1-Cpx metamorphic layering. **b** Enlargement of the main vein shown in (**a**), showing the mineralogical assemblages coexisting in the veins and consisting of poikiloblastic vesuvianite (*Ves*)-grandite garnet (Grs_2)-wollastonite (*Wo*) aggregates. **c** Photomicrograph showing the textural relationships between a foliation-parallel vein (*V*) and the host rock (*HR*). Note the crystallization of wollastonite (*Wo*) at the vein–host rock interface (*crossed polars*). **d** Hand specimen showing relationships between the peak metamorphic grossular(Grs_1)-rich layering, the foliation-parallel (V_{fp}) and the foliation-orthogonal (V_{fo}) veins. The latter are constituted by grandite garnet (Grs_2). Note the crystallisation of wollastonite (*Wo*) at the vein–host rock interface. **e** Field relationships showing mutual overprinting relationships between wollastonite-bearing foliation-parallel and foliation-perpendicular veins. **f** Photomicrograph showing the contact between massive garnet-clinopyroxene calc–silicates and marbles. Note how garnet (Grs_2)-bearing, subvertical foliation perpendicular veins flatten when approaching the marble–calc–silicate interface. The marbles show a granoblastic polygonal texture of calcite grains (*crossed Polars*)

The main difference between the fractures occurring in the marbles and in the underlying calc–silicate rocks concerns the fracture abundance (i.e. density). To evaluate this parameter, we used the circle-inventory method (Wheeler and Dickinson 1980). In this method, the fracture abundance (ρ_f) is defined as the total length of all fractures (L) within a significant (i.e. for the fracture abundance) inventory circle of radius r divided by the area of the circle itself (Fig. 5d, f), according the following expression:

$$\rho_f = L/\pi r^2, \quad (1)$$

where ρ_f is measured in units of length/area (hereafter referred to as mm^{-1}).

We calculated the fracture abundance in six selected sites, three in calc–silicates and three in the overlying marbles. Results show that the fracture abundance in calc–silicates is about one order of magnitude greater than that in marbles (Table 1).

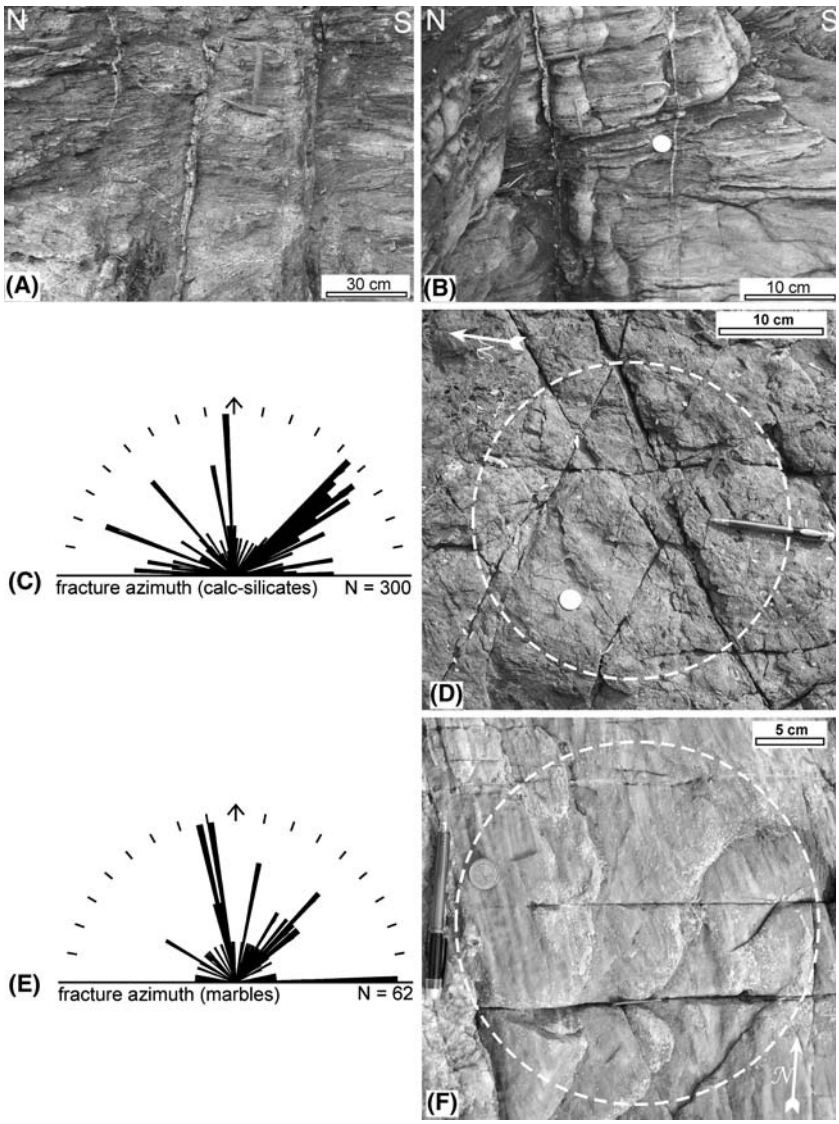

Fig. 5 Texturally-late quartz veins found in calc–silicates (**a**) and marbles (**b**). These veins are labelled in the text as Qtz_1 and Qtz_2, respectively. **c** Rose diagrams showing the cumulative distribution of fracture azimuths in calc–silicates. **d** Outcrop photograph of fracturing in calc–silicates. **e** Rose diagrams showing the cumulative distribution of fracture azimuths in marbles. **f** Outcrop photograph of fracturing in marbles. Note the inventory circles used to compute the fracture abundance in **d** and **f** (see Table 1)

Table 1 Fracture abundance

Rock type	No. of fractures	L (mm)	r (mm)	ρ_f (mm^{-1})
Calc–silicate	73	1506	63	0.120
Calc–silicate	158	9688	166	0.111
Calc–silicate	69	1723	66	0.125
Marble	20	2162	238	0.012
Marble	24	1536	138	0.025
Marble	18	1114	144	0.017

L = summed length of fractures falling within the inventory-circle; r = radius of the inventory-circle; ρ_f = fracture abundance

Mineral chemistry

Quantitative analyses were made of minerals in both the calc–silicate granofels and in the veins. Mineral compositions were obtained using a CAMECA SX 50 electron microprobe at the CNR laboratories of the University of Rome ''La Sapienza''. Analyses were done in point beam mode (5 μm in size) at 15 kV and 15 nA, using natural and synthetic phases as standards.

Recalculation of the mineral formulae and estimation of the Fe^{3+} content were made using the software AX2000 in the THERMOCALC package (Holland and Powell 1998). Representative analyses and structural formulae of minerals are presented in Table 2. All the mineral abbreviations used in this study are after Bucher and Frey (2002).

Garnet

In the granofelses, matrix (Grs_1) and vein (Grs_2) garnets are essentially grossular-andradite solid solutions (grandite garnets: $Adr_{13–27}Grs_{67–87}Alm_{1–4}$). The Grs zonation is generally weak, but most commonly decreases towards the rim, compensated by the increase

Table 2 Selected mineral analyses and structural formulae of mineral phases occurring at the metamorphic peak in the calc–silicate hornfels of the Procchio area, Elba Island

Mineral	Grt	Grt	Grt	Cpx	Cpx	Pl	Pl	Pl	K-fs	Vsv	Vsv
Comment	Grs_1-core	Grs_1-rim	Grs_2-vein	Matrix	Matrix	Matrix	Matrix	Matrix	Matrix	Matrix	Vein
Wt (%) oxides											
SiO_2	38.75	38.58	37.56	52.08	51.65	54.77	44.96	63.78	65.53	35.42	35.87
Al_2O_3	19.55	18.00	15.60	0.47	0.22	28.33	35.06	22.65	18.08	15.84	14.91
TiO_2	0.61	0.31	0.38	0.11	0.05	0.00	0.00	0.00	0.01	2.28	3.31
Cr_2O_3	0.05	0.01	0.00	0.01	0.09	0.00	0.00	0.00	0.00	0.00	0.00
FeO	5.01	7.35	7.19	12.67	17.42	0.08	0.17	0.00	0.11	4.21	4.61
MnO	0.15	0.17	0.29	0.23	0.45	0.00	0.07	0.07	0.00	0.04	0.07
MgO	0.21	0.14	0.14	9.97	7.05	0.00	0.00	0.01	0.01	1.45	1.46
CaO	35.85	35.74	35.10	23.86	23.13	10.68	18.37	4.00	0.00	35.04	35.05
Na_2O	0.03	0.01	0.04	0.07	0.17	5.19	1.11	9.37	1.11	0.08	0.17
K_2O	0.01	0.00	0.00	0.01	0.00	0.35	0.01	0.23	14.86	0.00	0.02
Σ	100.22	100.31	96.30	99.48	100.23	99.40	99.75	100.11	99.73	94.36	95.47
Cations	12(O)	12(O)	12(O)	6(O)	6(O)	8(O)	8(O)	8(O)	8(O)	30(O)	30(O)
Si	2.941	2.943	2.997	1.997	2.009	2.484	2.079	2.816	3.017	7.271	7.297
Al	1.749	1.619	1.468	0.021	0.010	1.514	1.911	1.179	0.981	3.833	3.576
Ti	0.035	0.018	0.023	0.003	0.001	0.000	0.000	0.000	0.000	0.352	0.506
Cr	0.003	0.001	0.000	0.000	0.000	0.00	0.000	0.000	0.000	0.000	0.000
Fe^{2+}	0.000	0.009	0.005	0.406	0.567	0.000	0.000	0.000	0.000	0.415	0.450
Fe^{3+}	0.302	0.460	0.475	0.000	0.000	0.003	0.009	0.000	0.004	0.277	0.300
Mn	0.007	0.011	0.020	0.007	0.015	0.000	0.003	0.002	0.000	0.007	0.012
Mg	0.010	0.016	0.017	0.570	0.409	0.000	0.003	0.001	0.000	0.444	0.443
Ca	2.915	2.922	3.001	0.980	0.964	0.519	0.910	0.189	0.000	7.707	7.640
Na	0.004	0.002	0.006	0.005	0.013	0.456	0.100	0.802	0.099	0.032	0.067
K	0.001	0.000	0.000	0.000	0.000	0.020	0.001	0.013	0.874	0.000	0.005
Grs activity	0.70 ± 0.11	0.60 ± 0.09	0.53 ± 0.08								
An activity						0.73 ± 0.04	0.91 ± 0.05	0.32± 0.03			
San activity									0.91± 0.03		

of the Adr component. In some of the foliation-perpendicular veins, garnet is usually hydrogrossular.

Clinopyroxene

Clinopyroxene found both in the matrix and as inclusions in garnets corresponds to diopside-henderbergite solid solutions ($Di_{57–64}Hd_{43–36}$), without any significant compositional variations.

Feldspar

Plagioclase within the garnet-bearing layers is invariably richer in anorthite ($An_{52–90}Ab_{8–46}Or_{0–2}$) than that found in the garnet-free calc–silicate portions ($An_{19–26}Ab_{73–80}Or_{0–1}$). K-feldspar contains up to 7–10% albite ($An_{0–1}Ab_{8–10}Or_{90–91}$). No chemical zoning is apparent in either of the feldspar types.

Vesuvianite

Vesuvianite typically shows a significant Ti content, with TiO_2 values up to 3.3 wt%.

Wollastonite, *calcite* and *quartz* contain no significant impurities.

Thermobarometry

The *P–T* conditions of contact metamorphism were estimated from mineral equilibria involving the coexisting mineral phases at the metamorphic peak in calc–silicates (Table 2). Position of the mineral reaction curves in the *P–T* space was calibrated with the software THERMOCALC (in the form of the July 2002 upgrade), using the data sets and activity formulations from the enclosed AX program (Table 2).

The presence of the muscovite-absent And-Kfs-Crd-Bt-Qtz assemblage in metapelites constrains the peak conditions within the andalusite stability field and up temperature of the muscovite–quartz breakdown reaction curve, which is regulated by the following reaction:

$$\mathrm{Ms} + \mathrm{Qtz} = \mathrm{And} + \mathrm{K\text{-}fs} + \mathrm{H_2O}. \quad (2)$$

Considering the appropriate activity of sanidine in K-fs (0.91; Table 2) and assuming simple end-member reactions in the KFMASH, this reaction restricts

conditions of metamorphism to $P < 2.5$ kbar at 550–700°C (reaction curve 1 in Fig. 6).

The occurrence of Grs, Wo, and Pl without Qtz in the peak assemblage found in the calc–silicates of the Procchio area makes it possible to constrain the peak T to values above the solid–solid Grs-Qtz-An-Wo equilibrium,

$$\text{Grs} + \text{Qtz} = \text{Pl} + 2\ \text{Wo}; \quad (3)$$

this equilibrium having a moderate positive dP/dT slope in the P–T space (e.g. Droop and Al–Filali 1996; Ferry et al. 2001). The expected temperature interval was obtained by combining the calculated activity of Grs_1 (0.60–0.70) with that of An (0.73–91) in plagioclase (Table 2), and considering unit activity of Wo and Qtz (reaction curves 2 in Fig. 6). Further constraints on peak temperatures were obtained from two-feldspar thermometry. Calculations using a range of solution models and mixing data were done by means of the software SOLVCALC (Wen and Nekvasil 1994 and references therein). Temperature estimates obtained using the An rich plagioclase compositions range from 550 to 625°C at 1 kbar, regardless of the solution model adopted. Estimations obtained using the An poor compositions are systematically lower (between 470 and 520°C), probably reflecting re-equilibration during progress of contact metamorphism.

Conditions of metamorphism therefore lie up temperature of the Grs-Qtz-An-Wo equilibrium (reaction curves 2 in Fig. 6), within the region defined by the andalusite–sillimanite boundary and the maximum temperature limit obtained from the feldspar thermometry, although this constraint varies depending on the choice of the aluminosilicate phase diagram. Considering the reconstructed thickness of the rock section above the Monte Capanne intrusion (Rocchi et al. 2002), reliable P–T estimates for the contact metamorphism in the Monte Capanne thermal aureole are thus T = 575–625°C at P = 1.5–2 kbar (Fig. 6).

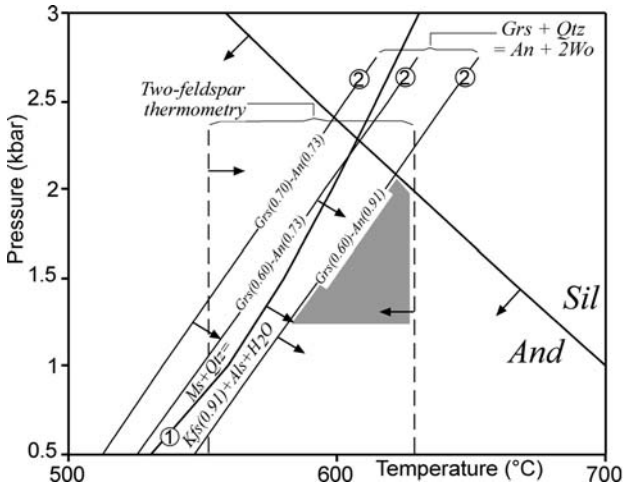

Fig. 6 Peak P–T metamorphic conditions (*shaded*) for the calcsilicate rocks of the contact aureole of the Monte Capanne pluton in the Procchio area. *Arrows* on curves used as P–T limits indicate field in which metamorphic conditions must lie. Curves for And-Sil and muscovite (*Ms*)–Quartz (*Qtz*)-K-feldspar (*Kfs*)-aluminium silicate (*Als*)-H_2O fluid equilibria assume all phases are pure substances except for Kfs, whose sanidine activity was set to 0.91. See text for further details

Fluid inclusion analysis

Fluid inclusion analysis was performed on minerals separated from (1) the calc–silicate hornfels rocks (samples PR; mineral: Ves and Grt), (2) the high-grade (both perpendicular and foliation parallel) vein systems (samples PRV1 and GRV; minerals: Ves and Grt), and (3) the late-stage Qtz_1 and Qtz_2 veins (samples PRV2; mineral: quartz). Conventional freezing and heating microthermometric analyses were carried out according to the procedure outlined in the Appendix. The laser-excited Raman spectral analysis was used to identify the composition of the gas phase in the different fluid inclusion types. Fluid inclusion data refer only to those fluid inclusions that we interpreted as having a primary origin, i.e. the fluid inclusions that occur isolated or in clusters. Primary clusters are usually found in the cores of the host minerals, but garnets often host fluid inclusion assemblages trapped within growth zoning. Pseudosecondary and secondary fluid inclusions typically occur along trails and planes and are not considered in this study.

Fluid inclusion populations hosted in garnet and vesuvianite (samples PR, PRV1 and GRV) consist of two distinct types (Fig. 7): (1) type-B, a highly-saline brine, both liquid (L)-rich and vapour (V)-rich fluid inclusions, containing a variable number of solids; and (2) type-V monophase V inclusions. Inclusion sizes range from ~5 to 50 μm. On the other hand, the late-stage Qtz_1 and Qtz_2 samples from the PRV2 veins contain only two-phase aqueous (L+V, L-rich) fluid inclusions.

Type-B fluid inclusions always contain a halite cube and usually several other solids. SEM-EDS analyses revealed that the salts consist mainly of Na and Cl, with significant amount of Ca and K. The small size of the inclusions and the presence of many solids, made equilibration temperature (T_e) measurement possible in only one case (i.e. at –50°C), confirming the presence of $CaCl_2$ in the fluid (Crawford 1981). Raman analyses defined the solids as Ca-Mg-carbonates and Ca-sulphates (see inset in Fig. 7). Based on these

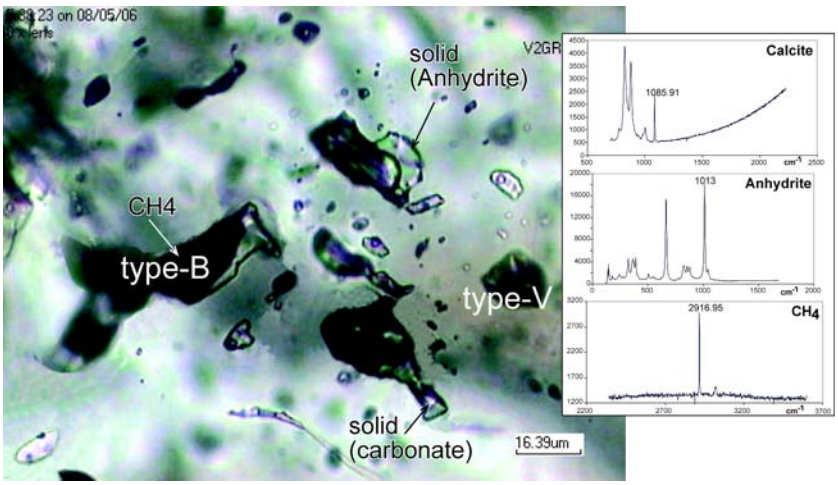

Fig. 7 Coeval entrapment of different types of fluid inclusions (type B and V) at the metamorphic peak in calc–silicates (host mineral is garnet). The *inset* shows the Raman spectra as obtained for the gas phase and for the solids within the inclusions (see text for further details). In many other inclusions, solids are Mg-carbonate

data, the fluid is a complex aqueous system composed of a H_2O-Na^+-K^+-Ca^{2+}-Mg^{2+}-Cl^--SO_4^{2-}-CO_3^{2-} mixture. Melting temperature for solids hosted within the inclusions (T_{ms}) were always (except for two cases) above the temperature of homogenisation between the liquid and the vapour phase (T_h), occurring at about 380°C (Fig. 8a). The T_{ms} equals the total homogenisation temperature (T_{htot}) and is grouped in the 550–600°C temperature interval (Fig. 8b). This temperature range provides salinities of the brine inclusions ranging from 50 to 66 wt% NaCl equivalent (Bodnar 2003 and references therein). Clathrates formed during microthermometric analyses and melted at about +6°C, suggesting the presence of gas species within the vapour phase. Raman analyses (about a hundred spots on the gas phase on both type-B and V fluid inclusions) defined the nature of the gas as CH_4 (see inset in Fig. 7). No homogenisation temperature was measured, probably because of the low density of the gas phase.

A completely different fluid occurs in the two-phase L+V, L-rich primary fluid inclusions hosted in quartz samples from the late stage veins. The trapped fluid is almost pure water ($T_{m\text{-}ice}$ around 0°C) with T_h providing a minimum trapping temperature of about 200°C.

Isotope data

Stable isotope data were obtained from 26 samples collected along two adjoining traverses perpendicular to the main foliation attitude across the calc–silicate rocks and the overlying marbles in the Procchio area (Fig. 2). Additional data were obtained from 19 samples taken from the calc–silicate rocks and the different vein generations. Calcite, garnet and quartz were analysed in this study, following the analytical procedure described in the Appendix. Results are shown on Tables 3 and 4.

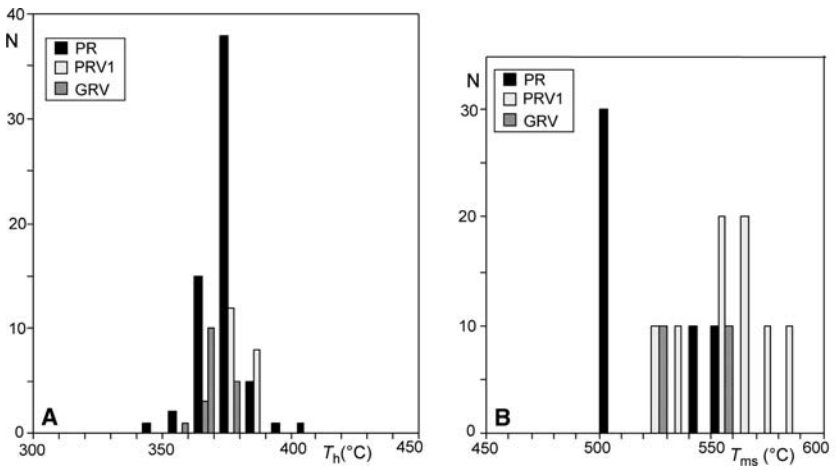

Fig. 8 Microthermometric data for fluid inclusion in mineral phases (Grt, Ves, Wo) coexisting at the metamorphic peak in the calc–silicates. **a** Histogram of liquid–vapour homogenisation temperatures (T_h). **b** Histogram of the melting temperature (T_{ms}) of solids hosted in the fluid inclusions

Table 3 Stable isotope data of calcite in selected samples taken along the calc–silicate/marble transition at Procchio, Elba Island

Sample	Rock type	δ^{13}C(PDB)‰	δ^{18}O (SMOW)‰	Δ(Cal-Grt$_H$)	Distance (m)
Samples taken along the 1st traverse					
C3	Calcsilicate	–1.38	15.39	3.43	–0.59
C4	Calcsilicate	–1.01	15.40	3.43	–0.39
C5	Calcsilicate	0.92	22.28	10.33	–0.24
C6	Calcsilicate	–0.24	17.02	5.06	–0.17
C7	Calcsilicate	0.18	17.62	5.67	–0.06
M8	Marble	1.83	24.29		0.06
M9	Marble	1.72	24.84		0.24
M10	Marble	1.78	24.85		0.50
M11	Marble	1.81	24.38		0.66
M12	Marble	1.19	23.69		0.71
M13	Marble	1.47	24.56		0.92
M14	Calcite boudin	0.98	24.54		0.95
M14	Marble	1.61	24.81		2.12
M15	Marble	0.82	25.36		3.42
Samples taken along the 2nd traverse					
M2–0	Marble	1.16	23.98		0.31
M2–1	Marble	0.51	23.36		0.60
M2–2	Marble	0.73	24.19		0.93
M2–4	Marble	1.49	24.25		1.19
M2–5	Marble	1.26	24.15		1.43
M2–6	Marble	0.62	23.15		1.75
M2–7	Marble	1.41	23.61		2.07
M2–8	Marble	2.05	24.26		2.30
M2–9	Marble	1.96	24.40		2.55
M2–10	Marble	1.98	24.32		2.88
M2–11	Marble	1.97	24.75		3.88
M2–12	Marble	1.94	24.33		4.88

Distance is measured perpendicular to main foliation from the marble/calc–silicate contact (positive values towards the top)

Table 4 Values of δ^{18}O (SMOW) and mineral fractionations of garnet and quartz in samples taken from the calc–silicate rocks

Sample	δ^{18}O (SMOW) ‰	Δ(Min-Grt$_H$)
Grt$_{H\text{-}1}$	12.47	
Grt$_{H\text{-}2}$	12.58	
Grt$_{H\text{-}3}$	10.96	
Grt$_{H\text{-}4}$	11.81	
Grt$_{V\text{-}1}$	11.17	–0.79
Grt$_{V\text{-}2}$	11.04	–0.92
Grt$_{V\text{-}3}$	11.30	–0.66
Grt$_{V\text{-}4}$	11.98	0.02
Grt$_{V\text{-}5}$	12.63	0.68
Grt$_{V\text{-}6}$	12.10	0.15
Grt$_{V\text{-}7}$	12.37	0.41
Qtz$_{1\text{–}1}$	24.37	12.42
Qtz$_{1\text{–}2}$	24.40	12.44
Qtz$_{1\text{–}3}$	24.38	12.42
Qtz$_{1\text{–}4}$	24.46	12.50
Qtz$_{2\text{–}1}$	6.27	–5.69
Qtz$_{2\text{–}2}$	6.25	–5.71
Qtz$_{2\text{–}3}$	6.05	–5.91
Qtz$_{2\text{–}4}$	6.07	–5.89

Grt$_H$ garnet from the host rock; *Grt$_V$* garnet from both the foliation-parallel and the foliation orthogonal veins; *Qtz$_1$* quartz from the hydrothermal Qtz$_1$ veins; *Qtz$_2$* quartz from the texturally-late Qtz$_2$ veins. Numbers refer to different samples

Isotope data on calcite

Calcite from the marble has δ^{13}C (Cal) values of 0.5–2.0‰ and δ^{18}O (Cal) of 23.1–24.7 ‰. Both δ^{13}C (Cal) and δ^{18}O (Cal) are nearly uniform in the marbles and do not show any significant variation with proximity to the contact with the calc–silicate rocks (Fig. 9; Table 3). These values are similar to the expected values of the precursor limestone (e.g. Hoefs 1997). On the other hand, calcite from the calc–silicate hornfelses has more variable composition for both carbon and oxygen isotopes. In general, the δ^{13}C(Cal) and δ^{18}O(Cal) values are systematically depleted in ^{13}C and ^{18}O relative to the unaltered marbles, with a lowering of ~2–4 and ~6–9‰, respectively (Fig. 9; Table 3). These depleted carbon and oxygen isotopic values are comparable to those obtained from other skarn deposits in analogous settings (e.g. Bowman 1998).

Isotope data on silicates

Garnet samples were separated from the host rock (Grt$_H$), the foliation-parallel and the foliation-perpendicular veins (Grt$_V$) (Fig. 4). Quartz samples were separated exclusively from the texturally-late, foliation-perpendicular Qtz$_1$ and Qtz$_2$ veins (Fig. 5a, b).

The $\delta^{18}O$(Grt) from the garnet samples are similar (values ranging from 11.0 to 12.6‰) regardless of their origin (i.e. host rocks or veins), suggesting that garnet constituted the main oxygen reservoir in the calc–silicates. The $\delta^{18}O(Qtz_1)$ values are very uniform at around the value of 24.4‰, whereas the $\delta^{18}O(Qtz_2)$ values show a mean value of 6.1‰ (Table 4).

The evaluation of the equilibrium conditions between minerals at the metamorphic peak in calc–silicates was made from the measured O-isotope fractionations. This was obtained by comparing the isotopic compositions of the different mineral phases with respect to the average $\delta^{18}O(Grt_H)$ value of 11.9‰ (σ = 0.7‰) that is considered as representative of the isotopic signature of the entire calc–silicate rock section (Fig. 10; Tables 3, 4). Excluding sample C5 (Table 3), the obtained $\Delta^{18}O$(Cal-Grt) values range between 3.4 and 5.6 and are not far from those expected at the peak temperature conditions of ~600°C (Zheng 1993). This suggests that the lowest $\delta^{18}O$ calcite in calc–silicates ($\delta^{18}O$(Cal) = 15.4–17.6) approached isotopic equilibrium with the skarn forming minerals (Fig. 10; Table 3). At about 200°C (the temperature obtained from the fluid inclusion analysis), quartz in isotopic equilibrium with Grt_H would result in a $\Delta^{18}O$(Qtz-Grt) value of about 13‰ (Valley et al. 2003), which is similar to that obtained from the Qtz_1 samples (Fig. 10; Table 4). On the other hand, at the same temperature of 200°C, Qtz_2 is not in equilibrium with the host rock garnet (Fig. 10), and the observed $\delta^{18}O(Qtz_2)$ can be attributed to precipitation of quartz from meteoric water (Clayton et al. 1972).

In summary, the following points arise from the isotopic study: (1) immediately adjacent to the marble/calc–silicate interface, carbon and oxygen isotopic shifts (up to 4 and 9‰, respectively) occur on a decimetre scale, attesting that the contact between marble and calc–silicate rocks is a major isotopic boundary; and (2) the isotopic fractionations suggest that the veins contain minerals that did not everywhere attain or approach the oxygen isotope equilibrium with the calc–silicate skarn. In particular, the $\delta^{18}O$(Qtz) values indicate a dramatic change in the nature of the circulating fluid phase during the episode of the Qtz_2 vein segregation.

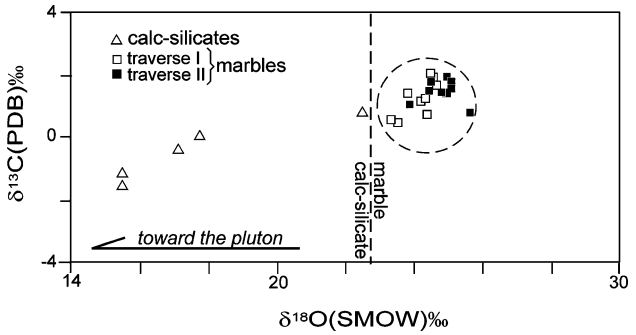

Fig. 9 Diagram of $\delta^{13}C$ (PDB) versus $\delta^{18}O$ (SMOW) of calcite taken along the marble/calc–silicate transition exposed at Procchio

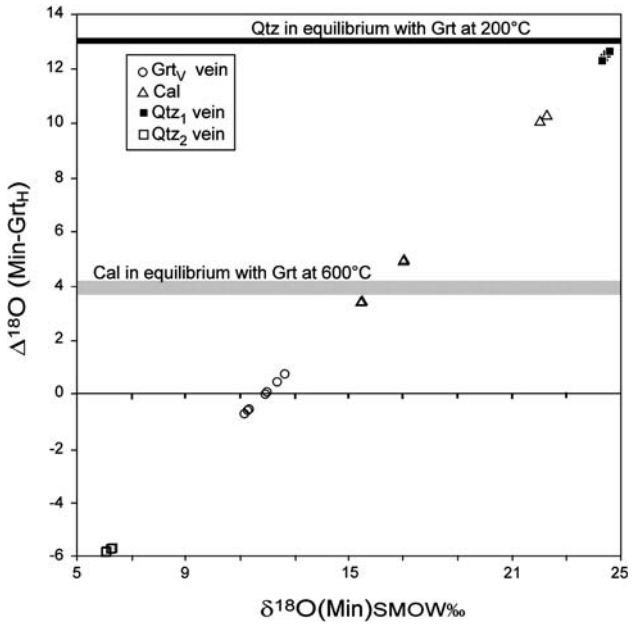

Fig. 10 Plot of $\Delta^{18}O$(Min-Grt_H) versus δ^{18}(Min) of the different mineral phases (Min) found both in veins (Grt and Qtz) and in the host rocks (Cal)

Discussion

The occurrence of wollastonite-bearing rocks in the inner aureole of the Monte Capanne pluton documents infiltration of chemically reactive fluids that preferentially flowed through the calc–silicate rocks (e.g. Ferry et al. 1998, 2001). Metamorphic assemblages are characterised by the coexistence of vesuvianite and epidote within the wollastonite zone, indicating extremely high H_2O/CO_2 conditions ($X(CO_2)_{fluid} < 0.05$) in the permeating fluids and, hence, demonstrating that the wollastonite-zone rocks were infiltrated by a great amount of aqueous fluids during the skarn mineralization (e.g. Nabelek et al. 1984; Nabelek 2002). On the other hand, the mineral assemblages found in the overlying diopside-grade marbles together with the lack of evidence of an isotopic shift indicate that fluid flow in the overlying marbles was very limited. This suggests that the marbles formed a closed or nearly closed system with respect to the fluid phase and that

fluid composition was internally buffered (see also Heinrich 1993; Nabelek 2002). Accordingly, the calc–silicate–marble contact (and hence the wollastonite reaction boundary) represents a major boundary between a high fluid–flux region on its high grade side (Wo and Grs zone) and a low fluid-flow one on its lower grade side (Cpx zone).

Fluid source

The mineral equilibria and the fluid inclusion data indicate that growth of the peak mineralogical assemblages occurred at $T \sim 600°C$, suggesting an intimate linkage between fluid production and the mineral zonation in the Monte Capanne inner aureole. The earliest fluids detected at the metamorphic peak of the wollastonite zone document that they consist of hypersaline brine coexisting with a CH_4 vapour phase, similarly to that already documented in other calc–silicate thermal aureoles (e.g. Heinrich 1993; Olsen and Ferry 1995). Infiltrating fluids are thus CO_2-free, although a large amount of CO_2 should have been produced through the wollastonite-forming reaction in the inner aureole:

$$\mathrm{Cal} + \mathrm{Qtz} \rightarrow \mathrm{Wo} + \mathrm{CO_2}. \quad (4)$$

This occurrence has been already reported by Heinrich (1993), who argued that CH_4 and CO_2 fluids never coexisted in calc–silicates, being CO_2 suddenly lost during the progress of the decarbonation reaction (4), which is primarily driven by the infiltrating aqueous fluids (e.g. Cui et al. 2003). Marbles are in fact impermeable to aqueous fluid infiltration (see e.g. Heinrich 1993; Buick and Cartwright 2002; Nabelek 2002; Cui et al. 2003), since calcite–calcite dihedral angles are unfavourable for pervasive grain boundary flow whereas they favour transit and removal of locally-generated CO_2–bearing fluids produced during decarbonation reactions (Holness and Graham 1995).

Textural relationships indicate that the brine and the vapour-rich CH_4–bearing inclusions were simultaneously trapped in the solvus H_2O-CH_4–salt (see also Heinrich 1993). In the H_2O-NaCl system, the immiscibility region is greatly increased by the addition of CH_4 (Duan 2003; Diamond 2003) and dramatically widens at the P–T conditions inferred for the metamorphic peak in the thermal aureole of the Monte Capanne pluton ($P < 2$ kbar and T~600°C; Lamb et al. 1996, 2002). It is well known that when magma crystallizes, immiscible fluids separate from the melt as high-density brine and low-density vapour (Candela 1989; Shinoara et al 1989; Cline and Bodnar 1991, 1994; Cline and Vanko 1995; Kelley and Früh-Green 2001; Heinrich et al. 2004). The cooling Monte Capanne pluton should have exsolved low $\delta^{18}O$ fluids, with $\delta^{18}O$ in the 6–15‰ range (Zheng and Hoefs 1993). In the calc–silicate inner aureole, the systematic depletion in the $\delta^{18}O$(Cal) values approaching the intrusion–wall rock contact suggests a high degree of recrystallization during infiltration of ^{18}O-depleted fluids. Furthermore, the constancy in the $\delta^{18}O$ values of garnet found both in veins and in the matrix calc–silicates (with an average value of 11.9‰; Table 4) suggests that progress of the decarbonation reactions occurred in a fluid-buffered open system that promoted isotopic exchange with a fluid exsolved directly from the crystallising Monte Capanne pluton.

Based on the arguments discussed above, we infer (1) that the felsic magma of the Monte Capanne was the source of fluid for skarn development in the Procchio area, and (2) that CH_4 was derived from C-bearing, highly saline magmatic fluids and trapped in fluid inclusions along with the brine (e.g. Kelley and Früh-Green 2001). In this context, precipitation of graphite in calc–silicates from C-bearing magmatic fluids should have thus occurred through the reaction (Luque et al. 1998):

$$\mathrm{CO_2} + \mathrm{CH_4} \rightarrow 2\mathrm{C} + 2\mathrm{H_2O}, \quad (5)$$

which produced at the same time a graphite-bearing aqueous fluid and the consumption of part of the gas (CO_2 + CH_4) exsolved from the magma. However, we can also not exclude a local source for CH_4 from the existing graphite through the reaction (Nabelek 2002):

$$2\mathrm{C} + 2\mathrm{H_2O} \rightarrow \mathrm{CO_2} + \mathrm{CH_4}, \quad (6)$$

which could have been promoted by the aqueous fluid infiltration in calc–silicates.

Despite the fact that there is some scatter in the data, the isotopic fractionations suggest that the circulating fluids shared the same cooling history as the aureole during the waning stage of the thermal metamorphism. This is attested by the fact that the low-temperature (T ~200 °C) fluids associated with the Qtz_1–bearing hydrothermal veins were in isotopic equilibrium ($\Delta^{18}(Qtz_1\text{–}Grt) = \sim 13‰$) with the calc–silicate host rocks during cooling of the Monte Capanne intrusion. On the other hand, the isotopic signature of the texturally-late Qtz_2 veins, documents a marked isotopic disequilibrium between the precipitating fluids and the calc–silicate host rocks (Fig. 10), indicating that the magmatic fluids were progressively replaced by fluids of meteoric origin that deeply circulated near the cooling intrusion.

Infiltration mechanism

In order to define the infiltration mechanism driving metasomatism and skarn formation in the inner thermal aureole of the Mount Capanne intrusion, we consider the following: (1) the infiltrated brines did not permeate the overlying marbles, and (2) the pathways of fluid flow are presently tracked in the field by distribution of the wollastonite-bearing rocks (Ferry et al. 1998, 2001; Nabelek 2002).

The patterns of wollastonite distribution in the calc–silicate rocks of the Procchio area show prominent evidence of fracture-controlled fluid flow during skarn formation, documenting that fracturing assisted mineral crystallization at the metamorphic peak; this process occurred despite inhibiting factors such as the elevated temperature (T~600°C). Wollastonite distribution also shows that the pre-metamorphic lithological contacts were zones of elevated permeability that favoured fluid access along the main planar, subhorizontal anisotropies parallel to the intrusion–host rocks contact. A notable component of fluid flow also occurred across layering, through subvertical fractures that cut through the calc–silicate layers.

The fracture systematics indicate a nearly radial pattern of fracturing and the fracture abundance abruptly decreases moving from the inner calc–silicate beds to the outer marbles. This sudden decrease of fracture abundance also corresponds to a concomitant decrease in the amount of veining that in marbles is limited only to low-temperature quartz segregations. Our data thus suggest that the contact between marble and calc–silicate rocks in addition to being a mineralogical and an isotopic boundary also constituted a major structural/rheological boundary, separating in the inner aureole brittle deforming rocks below from ductile deforming ones above.

The contrasting rheological behaviours of the marble and calc–silicate rocks can be primarily explained by considering the fact that modes of deformation in calc–silicates and marbles during pluton emplacement were dominated by garnet and calcite rheology, respectively. With garnet being much stronger than calcite in dry conditions (e.g. Ranalli 1995), the rheological contrast between these two minerals was responsible for the brittle fracturing of calc–silicates and the ductile flow in marbles as long as high temperatures were maintained during active deformation in the Monte Capanne thermal aureole. Pluton growth might have had a further impact on the modes of deformation of the calc–silicate inner aureole, because the occurrence of both tightly folded leucocratic dykes and radiating fractures set oriented perpendicular to the pluton/host rock margin suggests fast strain rates operating during emplacement of the Monte Capanne intrusion (see Johnson et al. 2001; Albertz et al. 2005). In this view, fast strain rate during emplacement-related deformation may have enhanced the brittle behaviour of the inner, high-strength calc–silicate aureole of the Procchio area.

We infer that after the metamorphic peak was attained in the thermal aureole, ductilely deformed marbles acted as barrier to fluids exsolved from the crystallizing intrusion, causing build up of the pore fluid pressure and promoting hydrofracturing (e.g. Norris and Henley 1976; Knapp and Knight 1977; Etheridge 1983; Connolly 1997; Cox et al. 2001) in the garnet-bearing calc–silicates. The occurrence of a rheological boundary acting as a barrier to fluids (see also Ord and Oliver 1997; Sibson and Scott 1998) coupled with fluid overpressuring is thus here interpreted as a major factor leading to hydrofracturing and, hence, to exotic fluid infiltration and skarn mineralization in calc–silicates (Fig. 11). Reaction-enhanced permeability resulting from the volume reduction of solids during decarbonation and devolatisation reactions could have also contributed to increase in the pore fluid pressure in calc–silicates (Rumble and Spear 1983; Yardley and Lloyd 1995; Connolly 1997; Marchildon and Dipple 1998), especially during the wollastonite-forming reactions (Zhang et al. 2000).

Once infiltration started, cyclic fluid pumping induced by active deformation during pluton emplacement should have enhanced some form of feedback between fluid production, hydrofracturing (and sealing) in calc–silicates and ductile flow in the marbles. Fluid infiltration dominantly occurred through layer (foliation)-parallel pathways that forced horizontal

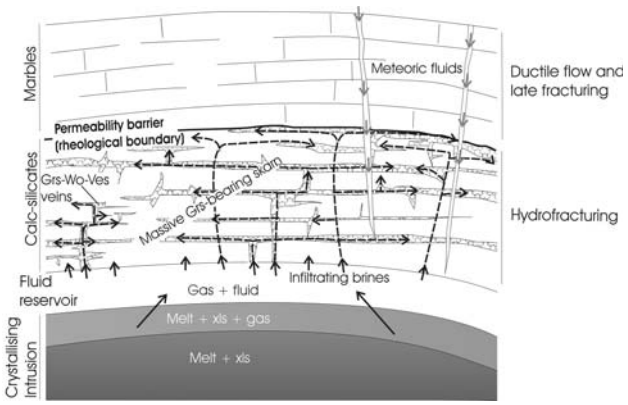

Fig. 11 Cartoon showing the pattern of fluid infiltration in the inner aureole of the Monte Capanne pluton. Fluid exsolved vertically from the pluton (*dashed black arrows*) flowed laterally in a channel defined by the more permeable calcsilicate rocks, sandwiched between pluton below and the impermeable marbles above (modified and re-adapted after Jamtveit et al. 1993)

fluid flow. This resulted in an interconnected fracture network, which provided an efficient permeability system for focusing fluids exsolved from the crystallizing Monte Capanne intrusion (Fig. 11). Cooling of the intrusive body caused the progressive embrittlement of the thermal aureole (Hanson 1995), determining the cessation of the rheological heterogeneity (the ductile-brittle boundary at the marble–calc–silicate interface) responsible for the maintenance of the pore fluid overpressure in the inner aureole. This resulted in diffuse fracturing of the thermal aureole, which caused the permeability increase in the marbles and infiltration of external (meteoric) fluids that progressively constituted the dominant fluids circulating in the inner aureole (Fig. 11). The paleohydrology of the thermal aureole surrounding the Monte Capanne intrusion thus documents a progressive transition from a magmatic fluid source to a meteoric one, such a process being controlled by the permeability distribution and evolution induced by the dynamics of the cooling intrusion (see also Hanson 1995).

This reconstruction may provide insights into the deep structure of the long-lasting (from about 3.8 Ma to the present) active geothermal fields of southern Tuscany (Mongelli et al. 1998) (Fig. 1). In particular, data from the thermal aureole of the Monte Capanne pluton suggest that the dominantly sub-horizontal permeability distribution in the deepest portions of the Larderello geothermal field (e.g. Cameli et al. 1993; Batini et al. 2003) likely corresponds to high-permeability horizons, where circulation of hot magmatic and/or metamorphic fluid is assisted by hydrofracturing (see also Vanorio et al. 2004). We infer that fluid overpressure responsible for hydrofracturing could be in part the consequence of vertical contrasts in the rheological properties of the basement rock hosting the geothermal field (alternating carbonate, calc–silicate and pelitic protoliths; Pandeli et al. 1991) that are maintained by the continuous advection of heat driven by multiple magma inputs from Pliocene onward (Dini et al. 2005). Active pluton emplacement in a lithologically heterogeneous rock section is thus here proposed as the major process responsible for both the maintenance of fluid overpressuring and the permeability creation through hydrofracturing at depth in the geothermal field of Larderello. In this scenario, the thermal and mechanical gradients associated with emplacement and cooling of the Pliocene–Pleistocene intrusives can be considered as a major cause for generating the fracture-controlled permeability field connecting the deep fluid reservoir with the surficial (meteoric) fluid circuit, and hence the maintenance of the hydrothermal circulation in the geothermal field.

Conclusions

The prograde metamorphic sequence described in the inner aureole of the Monte Capanne pluton documents infiltration of disequilibrium fluid exsolved from the cooling intrusion. These fluids permeated an initially dry thermometamorphic calcareous rock section along fracture-generated conduits, attesting structurally-controlled fluid flow during skarn formation in calc–silicates. Fluid flow was dominantly sub-horizontal, primarily controlled by the horizontal structures at the top of the pluton. Evolution of the thermal gradients in the contact aureole regulated the modes of deformation (ductile flow vs. fracturing) and, hence, the fracture-induced permeability creation and distribution within the aureole.

Three major results arise from this study: (1) a highly heterogeneous distribution of permeability (and hence heterogeneous fluid flow) is expected during pluton emplacement; (2) permeability distribution is primarily controlled by the rheological properties of the hosting rock section during transfer of heat and deformation induced by magma emplacement in the crust; and (3) the hydrodynamic regime at the pluton roof is dominated by horizontal fluid flow.

Acknowledgments We thank L. Minelli and G. Urru for their help during the fieldwork. M. Serracino is thanked for his help and kind assistance during microprobe analyses. M.L. Frezzotti is thanked for her help during Raman spectrometry analyses and advice. R. Funiciello is thanked for his continuous encouragement, support and advice. We thank F. Principi, E. Pandeli and M. Morelli for discussions in the field. We acknowledge Parco Nazionale dell'Arcipelago Toscano for giving us the possibility to work at Elba Island. Finally, we would like to thank an anonymous reviewer for the constructive and thoughtful revision that significantly contributed to improve the paper. Structural data analysis was carried out through the software DAISY.

Appendix: analytical techniques

Fluid inclusion analysis

Samples representative of the host rocks and of the different vein sets were prepared as 200 μm doubly-polished wafers. They were firstly observed with a polarizing microscope to define the types of fluid inclusions, the populations and their genetic relationships. Fluid inclusion analyses were done using: (1) microthermometry, (2) Raman laser microprobe, and (3) SEM-EDS analyses. Microthermometry was carried out by using a Linkam THMSG600 freezing–heating stage at the Istituto di Geologia Ambientale e Geoingegneria of CNR at the University of Roma ''La

Sapienza''. The calibration of the stage was made using pure natural CO_2 inclusions for low temperatures and synthetic fluid inclusions for high temperatures, respectively. Reproducibility of the triple point of CO_2 at –56.6°C was ±0.1°C. Low temperature (T_e, T_m) data were determined with a 0.5–1°C/min rate, whereas high temperature (T_h, T_{ms}) data with a heating rate of 5–10°C/min, respectively. A Confocal Labram Multichannel microspectrometre of the Jobin-Yvon ltd. at the Dipartimento di Scienze della Terra, Siena University, was used to collect Raman spectra. The 514.5 nm was used as excitation line by an Ar^+ ion laser. A Scanning Electron Microscope (SEM) study was also performed. The EDS spectra were obtained on opened fluid inclusions. Samples were prepared according to Salvi and William-Jones (1990). The composition of the powdery mass that precipitates inside the cavities was defined by means of EDS analyses. In few cases, solids inside the inclusions were also analyzed. Qualitative EDS analyses were performed using a Cameca SX50 electron microprobe fitted with 5 WDS spectrometers and 1 EDS Link eXL detector at the Istituto di Geologia Ambientale e Geoingegneria of CNR at the University of Roma ''La Sapienza''.

Isotope analysis

Analyses of calcites and silicate minerals were done at the laboratories of Mass Spectrometry at the Istituto di Geologia Ambientale e Geoingegneria of CNR at the University of Roma ''La Sapienza''. Oxygen isotope data of silicate samples were produced by laser fluorination (Sharp 1990), reacting 1.5–1.8 mg fragments in a F_2 gas atmosphere. A 15 W CO_2 laser, operating at a wavelength of 10.6 m to irradiate the samples, and pure fluorine desorbed at 320°C from hexafluoropotassium–nickelate salt (Asprey 1976) as a reagent were employed. The O_2 produced during laser fluorination was purified of excess fluorine and transferred to a cold finger with a 13 A molecular sieve. Further, oxygen gas purification was achieved by desorbing oxygen from the molecular sieve at –110°C using a liquid nitrogen–ethanol mixture. The purified gas was then transferred to a Finnigan Delta plus mass spectrometer for oxygen isotope analysis. A lab standard calibrated against NBS 28 standard was measured several times during the analysis session; its standard deviation after 15 repetitions is equal to 0.1. An amount of 100–150 μg of powdered calcium carbonate were used for oxygen and carbon isotope analysis. The extraction of CO_2 was done using the automated Kiel II - Finnigan carbonate device. The calcium carbonate reacted in phosphoric acid (H_3PO_4) at 72°C until all carbonate was completely digested; resultant CO_2 was purified of contaminant water vapour and then analyzed on a Finnigan Mat 252 mass spectrometer. Results are generally reproducible to ± 0.1‰ or better. The oxygen and carbon isotope compositions are reported as deviation in part per mil relative to the SMOW (*Standard Mean Oceanic Water*) and PDB (*Pee Dee Belemnite*) standards, respectively.

References

Albertz M, Paterson SR, Okaya D (2005) Fast strain rates during pluton emplacement: magmatically folded leucocratic dikes in aureoles of the Mount Stuart Batholith, Washington, and the Tuolumne Intrusive Suite, California. Geol Soc Am Bull 117:450–465

Asprey LB (1976) The preparation of very pure F_2 gas. J Fluor Chem 7:359–361

Barberi F, Innocenti F (1965) Le rocce cornubianitico-calcaree dell'anello termometamorfico del Monte Capanne (Isola d'Elba). Atti Società Toscana di Scienze Naturali 20:305–398

Barberi F, Giglia G, innocenti F, Marinelli, G Raggi G, Ricci CA, Squarci P, Taffi L Trevisan L (1967) Carta Geologica dell'Isola d'Elba, scale 1:25000, CNR, Rome

Batini F, Brogi A, Lazzarotto A, Liotta D, Pandeli E (2003) Geological features of Larderello-Travale and Mt. Amiata geothermal areas (Southern Tuscany, Italy). Episodes 26:239–244

Baumgartner LP, Ferry JM (1991) A model for coupled fluid-flow and mixed-volatile mineral reactions with applications to regional metamorphism. Contrib Mineral Petrol 106:273–285

Baumgartner LP, Gerdes ML, Person Roselle GT (1997) Porosity and permeability of carbonate rocks during contact metamorphism. In: Jamtveit B, Yardley BWD (eds) Fluid flow and transport in rocks: mechanisms and effects. Chapman and Hall, London, pp 83–98

Boccaletti M, Papini P (1989) Ricerche meso e microstrutturali sui corpi ignei neogenici della Toscana. 2: L'intrusione del Monte Capanne (Isola d'Elba). Boll Soc Geol Ital 108:699–710

Bodnar RJ (2003) Introduction to aqueous electrolyte fluid inclusions. In: Sampson I, Anderson A, Marshall D (eds) Fluid inclusions, analysis and interpretation. Mineralogical association of Canada, Short course 32: pp 81–100

Bortolotti V, Fazzuoli M, Pandeli E, Principi G, Babbini A, Corti S (2001) Geology of central and eastern Elba island, Italy. Ofioliti 26:97–150

Boullin JP, Bouchez JL, Lespinasse L, Pecher A (1993) Granite emplacement in extensional setting: an AMS study of the magmatic structures of Monte Capanne (Elba, Italy) Earth Planet Sci Lett 118:263–269

Bowman JR (1998) Stable isotope systematic of skarns. In: Lentz DL (ed) Mineralized Intrusion-related Skarn Systems. Mineralogical association of Canada, Short Course Series, 26 pp. 99–145

Bucher K, Frey M (2002) Petrogenesis of metamorphic rocks, 7th edn. Springer, Heidelberg

Buick IS, Cartwright I (2002) Fracture-controlled fluid flow and metasomatism in the contact aureole of the Marulan Batholith (New South Wales, Australia). Contrib Mineral Petrol 143:733–749

Cameli GM, Dini I, Liotta D (1993) Upper crustal structure of the Larderello geothermal field as a feature of post-collisional extensional tectonics, Southern Tuscany, Italy. Tectonophysics 224:413–423

Candela PA (1989) Magmatic ore-forming fluids: thermodynamics and mass transfer calculations of metal concentrations. Rev Econ Geol 4:203–221

Carmignani L, Decandia FA, Fantozzi PL, Lazzarotto A, Liotta D, Meccheri M (1994) Tertiary extensional tectonics in Tuscany (Northern Apennines, Italy). Tectonophysics 238:295–315

Cartwright I (1998) Permeability generation and resetting of tracers during contact metamorphic fluid flow: implications for advection-dispersion models. Contrib Mineral Petrol 140:163–179

Cartwright I, Buick IS (1996) Determining the direction of contact metamorphic fluid flow: an assessment of mineralogical and stable isotope criteria. J Metamorph Geol 14:289–305

Clayton RN, O'Neil JR, Mayeda TK (1972) Oxygen isotope exchange between quartz and water. J Geophys Res 77:3057–3067

Cline JS Bodnar RJ (1991) Can economic porphyry copper mineralization be generated by a ''typical'' calc-alkaline melt? J Geophys Res 96:8113–8126

Cline JS, Bodnar RJ (1994) Direct evolution of brine from a crystallizing silicic melt at the Questa, New Mexico, Molybdenum deposit. Econ Geol 89:1780–1802

Cline JS, Vanko DA (1995) Magmatically generated saline brines related to molybdenum at Questa, New Mexico, USA. In: Thompson JFH (ed) Magmas, fluids, and ore deposits. Mineralogical association of Canada, Ottawa, Short Course 23: pp 153–174

Connolly IAD (1997) Devolitization-generated fluid pressure and deformation-propagated fluid flow during prograde regional metamorphism. J Geophys Res 102:18149–18173

Cook SJ, Bowman JR (2000) Mineralogical evidence for fluid-rock interaction accompanying prograde contact metamorphism of siliceous dolomites: Alta stock Aureole, Utah, USA. J Petrol 41:739–757

Cox SF, Knackstedt MA, Braun J (2001) Principles of structural control on permeability and fluid flow in hydrothermal systems. Rev Econ Geol 11:1–24

Crawford ML (1981) Phase equilibria in aqueous fluid inclusions. In: Hollister LS, Crawford ML (eds) Fluid inclusions: applications to petrology. Mineralogical association of Canada, Ottawa, Short Course 6: pp 75–100

Cui X, Nabelek PI, Liu M (2001) Heat and fluid flow in contact metamorphic aureoles with layered and transient permeability, with application to the Notch Peak aureole, Utah. J Geophys Res 106:6477–6491

Cui X, Nabelek PI, Liu M (2003) Reactive flow of mixed CO2–HwO fluid and progress of calc–silicate reactions in contact metamorphic aureoles: insights from two-dimensional numerical modelling. J Metamorph Geol 21:663–684

Diamond LW (2003) Introduction to gas-bearing aqueous fluid inclusions. In: Sampson I, Anderson A, Marshall D (eds) Fluid inclusions, analysis and interpretation. Mineralogical association of Canada, Ottawa, Short Course 32: pp 101–158

Dickson MH, Fanelli M (2004) What is geothermal energy? http://www.iga.igg.cnr.it/geo/geoenergy.php

Dini A, Innocenti F, Rocchi S, Tonarini S, Westerman DS (2002) The magmatic evolution of the late Miocene laccolith–pluton–dyke granitic complex of Elba Island, Italy. Geol Mag 139:257–279

Dini A, Gianelli G, Puxeddu M, Ruggieri G (2005) Origin and evolution of Pliocene–Pleistocene granites from the Larderello geothermal field (Tuscan Magmatic Province, Italy). Lithos 81:1–31

Dipple GM, Ferry JM (1996) The effect of thermal history on the development of mineral assemblages during infiltration-driven contact metamorphism. Contrib Mineral Petrol 124:334–345

Droop GTR, Al-Filali IY (1996) Interaction of aqueous fluids with calcareous metasediments during high-T, low-P regional metamorphism in the Qadda area, southern Arabian Shield. J Metamorph Geol 14:613–634

Duan Z, Moller N, Weare JH (2003) Equations of state for the $NaCl$-H_2O-CH_4 system and the $NaCl$-H_2O-CO_2–CH_4 system: phase equilibria and volumetric properties above 573K. Geochim Cosmochim Acta 67:671–680

Dutrow B, Norton D (1995) Evolution of fluid pressure and fracture propagation during contact metamorphism. J Metamorph Geol 13:677–686

Etheridge MA (1983) Differential stress magnitudes during regional deformation and metamorphism: upper bound imposed by tensile fracturing. Geology 11:231–234

Ferry JM, Dipple GM (1992) Models for coupled fluid flow, mineral reaction and isotopic alteration during contact metamorphism: the Notch Peak aureole, Utah. Am Mineral 77:577–591

Ferry JM, Soresen SS, Rumble D (1998) Structurally controlled fluid flow during contact metamorphism in the Ritter Range pendant, California, USA. Contrib Mineral Petrol 130:358–378

Ferry JM, Wing BA, Rumble D III (2001) Formation of wollastonite by chemically reactive fluid flow during contact metamorphism, Mt Morrison Pendant, Sierra Nevada, California, USA. J Petrol 42:1705–1728

Ferry JM, Wing BA, Penniston-Dorland SC, Rumble D III (2002) The direction of fluid flow during contact metamorphism of siliceous carbonate rocks: new data for the Monzoni and Predazzo aureoles, northern Italy, and a global review. Contrib Mineral Petrol 142:679–699

Gianelli G, Manzella A, Puxeddu M (1997) Crustal models of the geothermal areas of southern Tuscany (Italy). Tectonophysics 281:221–239

Hanson RB (1995) The hydrodynamics of contact metamorphism. Geol Soc Am Bull 107:595–611

Heinrich W (1993) Fluid infiltration through metachert layers at the contact aureole of the Bufa del Diente intrusions, northeast Mexico: Implications for wollastonite formation and fluid immiscibility. Am Mineral 78:804–818

Heinrich W, Chukarov SS, Gottschalk M (2004) Mineral-fluid equilibria in the system CaO-MgO-SiO_2–H_2O-CO_2–$NaCl$ and the record of reactive fluid flow in contact metamorphic aureoles. Contrib Mineral Petrol 148:131–149

Hoefs J (1997) Stable isotope geochemistry, 4th edn. Springer, Heidelberg

Holland TJB, Powell R (1998) An internally consistent thermodynamic data set for phases of petrological interest. J Metamorph Geol 16:309–343

Holness MB, Graham CM (1995) P-T-X effects on equilibrium carbonate-H_2O-CO_2–$NaCl$ dihedral angles: constraints on carbonate permeability and the role of deformation during fluid infiltration. Contrib Mineral Petrol 119:301–313

Innocenti F, Serri G, Ferrara G, Manetti P, Tonarini S, (1992) Genesis and classification of the rocks of the Tuscan Magmatic Province: thirty years after the Marinelli's model. Acta Vulcanologica 2:247–265

Jamtveit B, Wogelius RA, Fraser DG (1993) Zonation patterns of skarn garnets: records of hydrothermal system evolution. Geology 21:113–116

Johnson SE, Albertz M, Paterson SR (2001) Growth rates of dike-fed plutons. are they compatible with observations in the middle and upper crust? Geology 29:727–730

Jolivet L, Faccenna C, Goffé B, Mattei M, Rossetti F, Brunet C, Storti F, Cadet JP, Funiciello R, D'Agostino N, Parra T (1998) Midcrustal shear zones in post-orogenic extension: example from the Northern Tyrrhenian Sea (Italy). J Geophys Res 103:12.123–12.160

Kelley DS, Fruh-Green GL (2001) Volatiles lines of descent in submarine plutonic environments: insights from stable isotope and fluid inclusion analyses. Geochim Cosmochim Acta 65:3325–3346

Knapp RB, Knight JE (1977) Differential thermal expansion of pore fluids: fracture propagation and micro earthquake production in hot pluton environment. J Geophys Res 82:2515–2522

Lamb WM, Popp RK, Boockoff LA (1996) The determination of phase relations in the CH_4–H_2O-NaCl system at 1 kbar, 400 to 600°C using synthetic fluid inclusions. Geochim Cosmochim Acta 60:1885–1897

Lamb WM, Mcshane CJ, Popp RK (2002) Phase relations in the CH_4–H_2O-NaCl system at 2 kbar, 300 to 600°C as determined using synthetic fluid inclusions. Geochim Cosmochim Acta 66:3971–3986

Luque FJ (1998) Natural fluid-deposited graphite; mineralogical characteristics and mechanisms of formation. Am J Sci 6:471–498

Marchildon N, Dipple GM (1998) Irregular isograds, reaction instabilities, and the evolution of permeability during metamorphism. Geology 26:15–18

Marinelli G (1967) Genèse des magmas du volcanisme Plio-Quaternaire des Apennines. Geol Rundsch 57:127–141

Mongelli F, Pialli G, Zito G (1998) Tectonic subsidence, heat flow and uplift in Tuscany: a new geodynamic and geothermal approach. Mem Soc Geol Ital 52:275–282

Nabelek PI. (2002) Calc-silicate reactions and bedding-controlled isotopic exchange in the Notch Peak aureole, Utah: implications for differential fluid fluxes with metamorphic grade. J Metamorph Geol 20:429–440

Nabelek PI, Labotka TC, O'Neil JR, Papike JJ (1984) Contrasting fluid/rock interaction between the Notch Peak granitic intrusion and argillites and limestones in western Utah: evidence from stable isotopes and phase assemblages. Contrib Mineral Petrol 86:25–34

Norris RJ, Henley RW (1976) Dewatering of a metamorphic pile. Geology 4:333–336

Norton D, Knight J (1977) Transport phenomena in hydrothermal systems: cooling plutons. Am J Sci 277:937–981

Oliver NSH (1996) Review and classification of structural controls on fluid flow during regional metamorphism. J Metamorph Geol 14:477–492

Oliver NSH (2001) Linking of regional and local hydrothermal systems in the mid-crust by shearing and faulting. Tectonophysics 335: 147–161

Olsen SN, Ferry JM (1995) A comparative fluid inclusion study of the Waterville and Sangerville (Vassalboro) formations, south-central Maine. Contrib Mineral Petrol 118:396–413

Ord A, Oliver NHS (1997) Mechanical controls on fluid flow during regional metamorphism: some numerical models. J Metamorph Geol 15:345–360

Pandeli E, Bertini G, Castellucci P (1991) The tectonic wedges complex of the Larderello area (southern Tuscany, Italy). Boll Soc Geol Ital 110:621–629

Peccerillo A (1999) Multiple mantle metasomatism in central-southern Italy: geochemical effects, timing and geodynamic implications. Geology 27:315–318

Ranalli G (1995) Rheology of the earth, 2nd edn. Chapman & Hall, London

Rocchi S, Westerman DS, Dini A, Innocenti F, Tonarini S (2002) Two-stage growth of laccoliths at Elba Island, Italy. Geology 30:983–986

Rumble D, Spear FS (1983) Oxigen-isotope equilibration and permeability enhancement during regional metamorphism. J Geol Soc Lond 140:619–628

Serri GF, Innocenti F, Manetti P (1993) Geochemical and petrological evidence of the subduction of delaminated Adriatic continental lithosphere in the genesis of the Neogene-Quaternary magmatism of central Italy. Tectonophysics 223:117–147

Sharp ZD (1990) In situ laser microprobe techniques for stable isotope analysis. Chem Geol 101:3–19

Shinohara H., Iiyama JT, Matsuo S (1989) Partition of chloride compounds between silicate melt and hydrothermal solutions: I - Partition of NaCl-KCl. Geochim Cosmochim Acta 53:2617–2630

Sibson RH, Scott J (1998) Stress/fault control on the containment and release of overpressured fluids: examples from gold-quartz vein systems in Juneau, Alaska; Victoria, Australia and Otago, New Zealand. Ore Geol Rev 13:293–306

Trevisan L (1950) L'Elba orientale e la sua tettonica di scivolamento per gravità. Memorie dell'Istituto di Geolologia dell'Università Padova 16:5–39

Valley JW, Bindeman IN, Peck WH (2003) Empirical calibration of oxygen isotope fractionation in zircon. Geochim Cosmochim Acta 67:3257–3266

Vanorio T, De Matteis R, Zollo A, Batini F, Fiordelisi A, Ciulli B (2004) The deep structure of the Larderello-Travale geothermal field from 3D microearthquake traveltime tomography. Geoph Res Lett 31:L07613, DOI:10.1029/2004GL019432, 2004

Velsker IV (2004) Liquid immiscibility and its role at the magmatic-hydrothermal transition: a summary of experimental studies. Chem Geol 210:7–31

Wen S, Nekvasil S (1994) SOLVCALC: an interactive graphics program package for calculating the ternary feldspar solvus and for two-feldspar geothermometry. Comp Geosci 20:1025–1040

Wheeler RL, Dickson JM (1980) Intensity of systematic joints, methods and applications. Geology 8:230–233

Zhang S, Fitzgerald JD, Cox SF (2000) Reaction-enhanced permeability during decarbonation of calcite + quartz $\rightarrow$ wollastonite + carbon dioxide. Geology 28:911–914

Zheng YF (1993) Calculation of oxygen isotope fractionation in anhydrous silicate minerals. Geochim Cosmochim Acta 57:1079–1091

Zheng YF, Hoefs J (1993) Carbon and oxygen covariations in hydrothermal calcites: theoretical modelling on mixing processes and application to Pb-Zn deposits in the Harz Mountains. Germany Min Dep 28:79–89